Research Article

Cancer Immunology Research

CAR-T Cells Surface-Engineered with Drug-Encapsulated Nanoparticles Can Ameliorate Intratumoral T-cell Hypofunction

Natnaree Siriwon[1], Yu Jeong Kim[2], Elizabeth Siegler[3], Xianhui Chen[2], Jennifer A. Rohrs[3], Yarong Liu[4], and Pin Wang[1,2,3]

Abstract

One limiting factor of CAR T-cell therapy for treatment of solid cancers is the suppressive tumor microenvironment (TME), which inactivates the function of tumor-infiltrating lymphocytes (TIL) through the production of immunosuppressive molecules, such as adenosine. Adenosine inhibits the function of $CD4^+$ and $CD8^+$ T cells by binding to and activating the A2a adenosine receptor (A2aR) expressed on their surface. This suppression pathway can be blocked using the A2aR-specific small molecule antagonist SCH-58261 (SCH), but its applications have been limited owing to difficulties delivering this drug to immune cells within the TME. To overcome this limitation, we used CAR-engineered T cells as active chaperones to deliver SCH-loaded cross-linked, multilamellar liposomal vesicles (cMLV) to tumor-infiltrating T cells deep within the immune suppressive TME. Through *in vitro* and *in vivo* studies, we have demonstrated that this system can be used to effectively deliver SCH to the TME. This treatment may prevent or rescue the emergence of hypofunctional CAR-T cells within the TME. *Cancer Immunol Res; 6(7); 812–24. ©2018 AACR.*

Introduction

Chimeric antigen receptor (CAR)-engineered T (CAR-T) cell therapy has demonstrated success in treating hematologic cancers, such as leukemia and B-cell lymphoma, in preclinical and clinical trials (1–3). This success has not been translated to the treatment of solid tumors (4–6). Unlike hematologic cancers, which circulate throughout the body in the blood stream, solid tumors have their own complex tumor microenvironment (TME), which provides a unique barrier to immunotherapy (7, 8). To be effective, immune cells must efficiently infiltrate the solid tumor mass and have extended persistence of *in vivo* expanded cells (9, 10). The TME contains a variety of protumorigenic factors that work to both prevent cancer-killing immune cells from entering the tumor area and dampen the activation of tumor infiltrating lymphocytes (TIL; refs. 8, 11). Many of these immune suppressive mechanisms can also negatively impact adoptively transferred CAR-T cells.

One of the underlying mechanisms responsible for the progressive loss of TIL function in the TME is an inhibitory pathway involving the A2a adenosine receptor (A2aR) expressed on the surface of activated T cells (12–14). The A2aR pathway is triggered by abnormally high concentrations of the extracellular immunosuppressive molecule adenosine, which has been reported to suppress T-cell proliferation and IFNγ secretion (15, 16). In the TME, extracellular adenosine triphosphate (ATP) is released in response to tissue damage and cellular stress. ATP in the extracellular environment is converted into adenosine by ectonucleases CD39 and CD73, which are upregulated in the hypoxic TME (17). Overexpression of CD73 has been observed in multiple aggressive cancers, conferring resistance to antitumor agents (18). Binding of adenosine to A2aR leads to increased intracellular cyclic AMP (cAMP) production in TILs. Elevation of intracellular cAMP induces activation of protein kinase A (PKA) and phosphorylation of the cAMP response element binding protein (CREB), which, in turn, abrogates T-cell receptor (TCR) signaling and IFNγ production by reducing the activity of the Akt pathway and inhibiting NF-kB–mediated immune activation (13, 18).

Studies have demonstrated that blocking A2aR signaling through either pharmacologic inhibition or genetic deletion can significantly improve antitumor immunity by enhancing the cytotoxic function of T and natural killer (NK) cells (12, 14, 15, 19). SCH-58261 (SCH) is one of the most selective and potent antagonists of A2aR (20). Despite its therapeutic potential, the clinical application of SCH has been hindered by the drug's poor solubility and suboptimal *in vivo* pharmacokinetic profile (21). Small-molecule drugs like SCH, which act directly on CAR-T cells, need to be maintained at high concentrations near their site of action in order to be effective. Thus, a carrier capable of regulating drug circulation time *in vivo* and efficiently delivering the drug to CAR-T cells in tumors, while minimizing delivery to other tissue/organ sites, is desired.

Advances in drug-delivery nanotechnology have enhanced the therapeutic efficacy of several anticancer drugs. Compared with free drugs, drug-loaded nanoparticles can improve targeted delivery by prolonging blood circulation time, controlling and

[1]Mork Family Department of Chemical Engineering and Materials Science, University of Southern California, Los Angeles, California. [2]Department of Pharmacology and Pharmaceutical Sciences, University of Southern California, Los Angeles, California. [3]Department of Biomedical Engineering, University of Southern California, Los Angeles, California. [4]R&D Department, HRAIN Biotechnology Co. Ltd., Shanghai, China.

Note: Supplementary data for this article are available at Cancer Immunology Research Online (http://cancerimmunolres.aacrjournals.org/).

N. Siriwon and Y.J. Kim contributed equally to this article.

Corresponding Author: Pin Wang, University of Southern California, 3710 McClintock Avenue, RTH506, Los Angeles, CA 90089. Phone: 213-740-0780; Fax: 213-740-8053; E-mail: pinwang@usc.edu

doi: 10.1158/2326-6066.CIR-17-0502

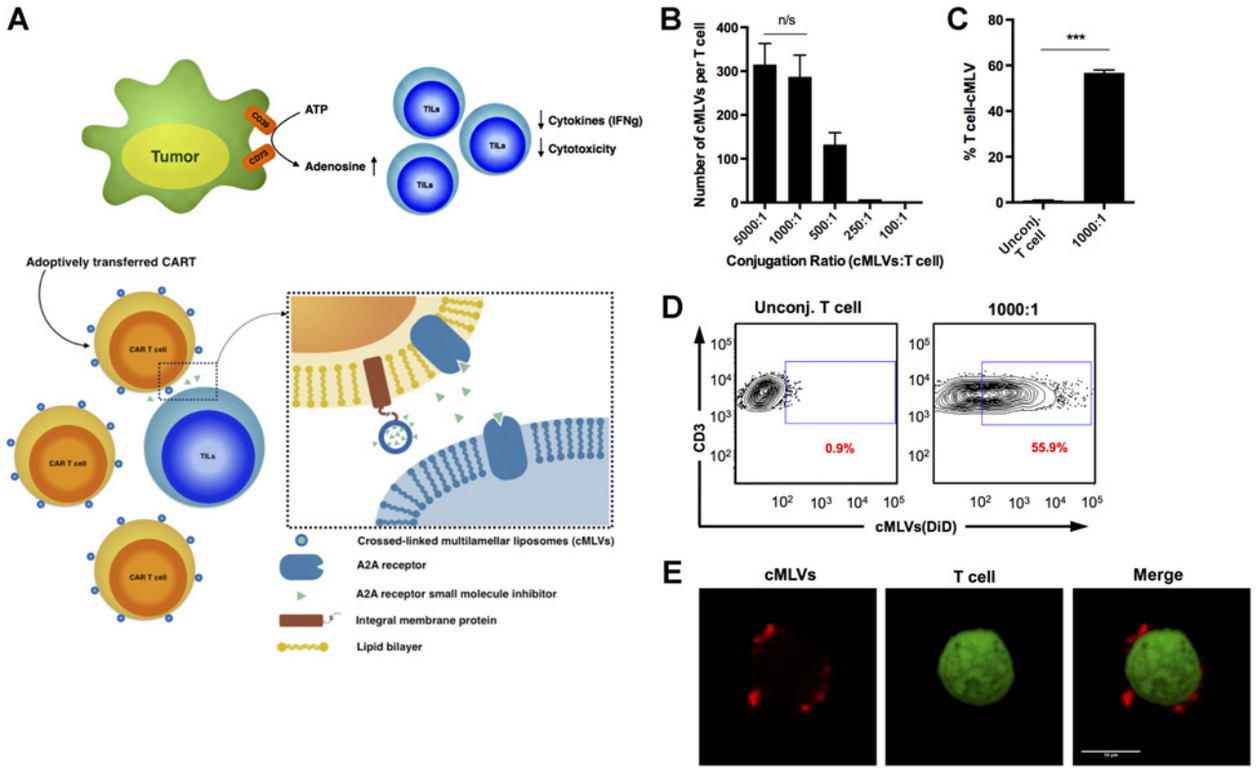

Figure 1.

Stable conjugation of cMLVs. **A,** Schematic diagram of cMLV-conjugated CAR-T cells in the presence of recipient cells *in vivo*. Maleimide functionalized cMLVs loaded with A2AR small-molecule inhibitors were conjugated to CAR-T cells via cell surface thiols. **B,** Number of conjugated cMLVs per T cell at different conjugation ratios. DiD fluorescence was analyzed to calculate the number of cMLVs on the surface of each cell. **C,** Percentage of $CD3^+$ T cells conjugated with cMLVs at 1,000:1 (cMLV:T cell) conjugation ratio. **D,** Representative flow cytometry analysis of percent cMLV conjugated $CD3^+$ T cells. **E,** Single-cell confocal microscopy images of DiD-loaded cMLV-conjugated CAR-T cells labeled with 1 μmol/L CFSE and washed with PBS prior to conjugation to cMLV(DiD). Scale bar, 10 μm. Red: DiD labeled cMLVs; green: CFSE labeled CAR T cell. All data are representative of three independent experiments. $n = 3$ samples per group; mean ± SD; n/s: not significant; *, $P < 0.05$; **, $P < 0.01$; ***, $P < 0.001$, one-way ANOVA with Tukey multiple comparison.

sustaining drug release profiles, and increasing drug concentration in the tumor through the enhanced permeability and retention (EPR) effect (22). The EPR effect is dependent on adequate vascularization of tumors, which may be completely lacking in some tumors that exhibit poor blood supply and hypoxia (23). High interstitial fluid pressures within the tumor can act to transport therapeutics back into the bloodstream. Most administered nanoparticles (up to 95%) are reported to accumulate in organs other than the tumor, including, the liver, spleen, and lungs (22). Hence, efficient delivery and distribution of nanoparticles within the tumor mass remains challenging.

Numerous studies have shown that the addition of targeting moieties on nanoparticles can significantly improve their tumor specificity and accumulation, but these targeting strategies still rely on passive distribution of the nanoparticles through the bloodstream (24). More advanced strategies have been explored, such as the use of immune cells as nanoparticle "chaperones" for targeted delivery and active transport into tumors (25, 26). Studies have shown that these immune delivery cells can provide effective treatment of tumors by facilitating drug delivery through active cellular migration and extravasation in response to chemoattractant gradients around the tumor and inflammatory sites (25–27). We believe that this delivery approach can be applied to alter interactions between the TME and endogenous or infused immune cells *in vivo*.

Therefore, we herein report an approach that enhanced the efficacy of CAR T-cell therapy by chemical conjugation of adjuvant drug–loaded cross-linked multilamellar liposomes (cMLV) that were maleimide-functionalized to the surface of CAR-T cells *ex vivo* prior to systemic administration (Fig. 1A). We demonstrated that cMLV nanoparticles could be covalently attached to CAR-T cells without affecting the cells' viability and effector functions. We further revealed that the therapeutic potential of CAR-T cells could be improved upon surface engineering with SCH-encapsulated cMLVs.

Materials and Methods

Mice

Female NOD.Cg-Prkdc^{scid}IL2Rγ^{tm1Wjl}/SZ (NSG) mice (6 to 10 weeks old) were purchased from The Jackson Laboratory. All animal studies were performed in accordance with the Animal Care and Use Committee guidelines of the NIH and were conducted under protocols approved by the Institutional Animal Care and Use Committee at the University of Southern California.

Cell culture, reagents, and antibodies

The 293T cell line (ATCC CRL-3216) was purchased and authenticated from ATCC. 293T cell culture was maintained in DMEM with 10% FBS, 2 mmol/L L-glutamine, penicillin (100 U/mL), streptomycin (100 μg/mL), and Normocin (100 μg/mL; InvivoGen). The human ovarian cancer cell line SKOV3 (ATCC HTB-77) and the human chronic myelogenous leukemia cell line K562 (ATCC CCL-243) were purchased and authenticated from ATCC. The cells were maintained in RPMI-1640 with 10% FBS, 2 mmol/L L-glutamine, 10 mmol/L HEPES, penicillin (100 U/mL), streptomycin (100 μg/mL), and Normocin (100 μg/mL; InvivoGen). All the above cell culture reagents were purchased from Hyclone. All cell lines were maintained in culture for 4 to 7 days before use. K562.CD19 and SKOV3.CD19 cells were generated by transducing parental K562 and SKOV3 cells with lentiviral FUW plasmid encoding the cDNA of human CD19 (28). All cells were routinely tested for potential mycoplasma contamination using the MycoSensor qPCR assay kit (Agilent Technologies).

SCH-58261 was purchased from Sigma-Aldrich. All lipids were purchased from NOF Corporation: 1,2-dioleoyl-sn-glycero-3-phosphocholine (DOPC), 1,2-dioleoyl-sn-glycero-3-phospho-(10-rac-glycerol; DOPG), and 1,2-dioleoyl-sn-glycero-3-phosphoethanolamine-N-[4-(p-maleimidophenyl)but-yramide (maleimide-headgroup lipid, MPB-PE).

Primary antibodies used in this study include: (i) anti-HA tag from Abcam (ab9110); (ii) Alexa Fluor 488–anti-phospho-CREB (clone 87G3) from Cell Signaling Technology; (iii) PE–anti-hCD45 (clone HI30), APC–anti-hCD45 (clone HI30), PE-Cy5.5–anti-hCD3 (clone HIT3a), FITC–anti-hCD4 (clone RPAT4), Pacific Blue–anti-hCD8 (clone SK1), FITC–anti-hCD8 (clone SK1), PE–anti-IFNγ (clone B27), APC–anti-EGFR (clone AY13), and Brilliant Violet 421–anti-hKi-67 (clone Ki-67), all from BioLegend; and (iv) Alexa Fluor 647 goat anti-rabbit from Thermo Fisher Scientific.

Preparation of T cells for adoptive transfer and viral transduction

Frozen human peripheral blood mononuclear cells (PBMC) were obtained from AllCells. Thawed PBMCs were cultured in T-cell medium (TCM) containing X-VIVO 15 serum-free medium (Lonza), 5% (vol/vol) GemCell human serum antibody AB (Gemini Bio-Products), 1% (vol/vol) glutamax-100× (Gibco, Life Technologies), 10 mmol/L HEPES buffer (Corning), 1% (vol/vol) penicillin/streptomycin (Corning), and 12.25 mmol/L *N*-acetyl-L-cysteine (Sigma-Aldrich). The culture was supplemented with human IL2 (10 ng/mL; PeproTech). The PBMCs were activated and expanded using Dynabeads human T-expander CD3/CD28 (Invitrogen) at a bead:PBMC ratio of 3:1. Activated PBMCs were transduced with viral vectors 48 hours after activation, as described below ("Lentiviral and retroviral vector preparation and transduction"). During *ex vivo* expansion, culture medium was replenished every 48 hours, and the T-cell density was maintained between 0.5×10^6 and 1×10^6 cells/mL.

Plasmid construction

The lentiviral vector encoding the HA-tagged CD19scFv-28-ζ CAR was constructed based on the CD19 CAR previously reported (29). The CD19 single-chain fragment variable (scFv) sequence, followed by the human CD8 hinge region (aa 138–184), was codon optimized and synthesized by Integrated DNA Technologies (Supplementary Table S1A). The CD19/CD8 hinge gene block was combined with the transmembrane and intracellular domains of human CD28 (aa 153–220) and the intracellular domain of human CD3ζ (aa 52–164) using PCR (Supplementary Table S1B and S1C). The CD8 leader sequence and HA-tag were inserted upstream of the CD19 scFv to allow for labeling and detection of CAR-expressing cells. To make the lentiviral vector, this sequence was inserted downstream of the human ubiquitin-C promoter in the lentiviral plasmid pFUW using Gibson assembly (28).

The retroviral vector encoding the same CD19 CAR sequence was kindly provided by Prof. Wolfgang Uckert (Humboldt University Berlin, Germany; ref. 30). The cDNAs of CD19 CAR and truncated EGFR (tEGFR) linked by a 2A sequence were inserted into the MP71 vector to yield the retroviral vectors for making CART.tEGFR cells.

Lentiviral and retroviral vector preparation and transduction

Lentiviral vectors were prepared by transient transfection of 293T cells using a standard calcium phosphate precipitation protocol (28). 293T cells were seeded at 18 million per 15 cm tissue culture dish (BD Biosciences) and were cotransfected with 40 μg of the lentiviral backbone plasmid, 20 μg of the VSV-G-encoding envelope plasmid, and 20 μg of the packaging plasmids (pMDLg/pRRE and pRSV-Rev). The viral supernatants were harvested 48 hours after transfection and filtered through a 0.45-μm filter (Corning). Two milliliters of the virus supernatant was loaded into a 24-well plate, with 5×10^5 activated human T cells and centrifuged for 90 minutes at $1{,}050 \times g$ at 25°C.

Retroviral vectors were prepared by transient transfection of 293T cells using a standard calcium phosphate precipitation protocol. 293T cells cultured in 15 cm tissue culture dishes were transfected with 37.5 μg of the retroviral backbone plasmid, along with 18.75 μg of the envelope plasmid pRD114, and 30 μg of the packaging plasmid encoding gag-pol. Activated human T cells were transduced and expanded (31). During cell expansion, T cells were resuspended at the concentration of 5×10^5 cells/mL with fresh TCM complemented with recombinant human IL2 (10 ng/mL; PeproTech). During *ex vivo* expansion, culture medium was replenished and cell density was adjusted to 5×10^5 cells/mL every 2 days.

Detection of receptor expression on T-cell surface

HA-tagged CD19scFv-28-ζ CAR-T cells were washed with PBS and stained with rabbit anti-HA followed by Alexa Fluor 647 goat anti-rabbit for CAR detection. Retrovirus-transduced cells were stained with APC-conjugated anti-hEGFR for tEGFR detection. Fluorescence was assessed using a MACSquant cytometer (Miltenyi Biotec), and all the FACS data were analyzed using FlowJo software version 9.3.2 (TreeStar).

Synthesis of nanoparticles and drug encapsulation

Liposomes were prepared based on the established dehydration-rehydration method previously reported (32). Briefly, cMLVs were prepared from 1.5 μmol of lipids at the molar ratio of the lipid composition of DOPC:DOPG:MPB-PE = 40:10:50. Then, the lipids were mixed in chloroform and evaporated under argon gas before drying under a vacuum overnight to form dried lipid films. The lipid film was rehydrated in 10 mmol/L Bis–Tris propane at pH 7.0. After the lipid was mixed through vigorous vortexing every 10 minutes for 1 hour, they underwent three

cycles of 15-second sonication (Misonix Microson XL2000) and rested on ice at 1-minute intervals after each cycle. A final concentration of 10 mmol/L $MgCl_2$ was added to induce divalent-triggered vesicle fusion. The crosslinking of multilamellar vesicles (cMLV) was performed by addition of dithiothreitol (DTT; Sigma-Aldrich) at a final concentration of 1.5 mmol/L for 1 hour at 37°C. The cMLVs were collected by centrifugation at 14,000 × *g* for 5 minutes and washed twice with PBS. For pegylation of cMLVs, the liposomes were further incubated with 1 mmol of 2 kDa mPEG-SH. To encapsulate SCH-58261 into cMLVs (cMLV(SCH)), 1 mg of SCH in organic solvent was mixed with the lipid mixture to form dried thin lipid films. To label liposome particles with 1,1′-dioctadecyl-3,3,3′,3′-tetramethylindodicarbocyanine (DiD; Invitrogen) lipophilic dyes, DiD dyes were added to the lipid mixture in chloroform at a ratio of 0.01:1 molar ratio (DiD: lipids). Morphology of multilamellar structure of the vesicles was analyzed and confirmed by cryo-electron microscopy, as in previous studies (32, 33). The hydrodynamic size of cMLVs was measured by dynamic light scattering (DLS; Wyatt Technology). The particles were suspended in filtered water, vortexed, and sonicated prior to analysis.

Nanoparticle conjugation with cells and *in situ* PEGylation

Chemical conjugation of nanoparticles to the T cells was performed based on a method reported by Stephan and colleagues (26). T cells were resuspended in serum-free X-vivo 15 medium (Lonza) at the concentration 10×10^6 cells/mL. An equal volume of nanoparticles in nuclease-free water were added to the cells and incubated for 30 minutes at 37°C with gentle agitation every 10 minutes. After a PBS wash to eliminate unbound particles, the residual maleimide groups were quenched by incubation of 10×10^6 cells/mL with thiol-terminated 2 kDA PEG (1 mg/mL) at 37°C for 30 minutes in complete RPMI medium, followed by two PBS washes to remove unbound PEG. For quantification of cell-bound particles, nanoparticles were labeled with the lipid-like fluorescent dye DiD before conjugation. Fluorescence was assessed using the MACSquant cytometer (Miltenyi Biotec) and a microplate reader. The surface conjugation of DiD-labeled cMLVs and carboxyfluorescein diacetate succinimide ester (CFSE)-labeled CAR-T cells was further visualized using confocal microscopy.

In vitro drug encapsulation and release

The amount of encapsulated SCH-58261 in the cMLV(SCH) was evaluated by C-18 reverse-phase high-performance liquid chromatography (RPHPLC; Beckman Coulter), as previously reported (33, 34). To obtain the release kinetics of SCH from cMLVs before and after cell conjugation, cMLV(SCH) and CAR-T cells conjugated to SCH-loaded cMLVs (CART.cMLV(SCH)) were incubated at 37°C in 10% FBS supplemented media, and replenished with fresh media daily. SCH was quantified from the harvested media every day for 5 days by HPLC.

Cytotoxicity assay

A modified version of a cytotoxicity assay was performed, as previously described in the study by Kochenderfer and colleagues, to assess the cytotoxicity of CAR-modified T cells (35). Nontarget cells, SKOV3 cells, and K562 cells were stained with the fluorescent dye 5-(and-6)-(((4-chloromethyl)benzoyl)amino) tetramethylrhodamine (CMTMR; Invitrogen). Target cells (SKOV3.CD19 and K562.CD19) were stained with CFSE (Invitrogen). The cultures were set up in triplicate in a sterile 96-well round bottom plate (Corning) at effector:target (E:T) cell ratios of 20:1, 10:1, 5:1, and 1:1. Immediately after 4 hours of incubation, 7-aminoactinomycin D (7AAD; BD Pharmingen) was added, as recommended by the manufacturer. The fluorescence was analyzed by flow cytometry. Cell cytotoxicity was calculated as [$CFSE^+7AAD^+$ cells/($CFSE^+7AAD^- + CFSE^+7AAD^+$)] cells.

Transmigration assay

T-cell transmigration assays were performed in 24-mm diameter, 3-μm pore size transwell plates (Costar). cMLV-conjugated and unconjugated CAR-T cells (0.5×10^6 cells/well) were plated on the upper wells, and TCM was added to the lower wells. The T-cell chemoattractant CXCL9 (100 ng/mL; PeproTech, Rocky Hill, NJ) was added to the lower wells. After incubation at 37°C for 6 hours, T cells that migrated into the lower chamber were counted.

In vivo biodistribution study

For the *in vivo* nanoparticle biodistribution study, a xenograft tumor model was used. To establish tumors, SKOV3.CD19 cells (3×10^6) in PBS solution were injected subcutaneously into the flanks of NSG mice. The mice were randomly assigned to treatment groups with 3 mice in each group. The mice received treatments when the tumor size reached 80 to 100 mm^3. DiD-labeled cMLVs (cMLVs; 1.5×10^9 particles), CD19 CAR-T cells (5×10^6) mixed with DiD-labeled cMLVs (CART+cMLV), CD19 CAR-T cells (5×10^6) surface-conjugated with DiD-labeled cMLVs (CART.cMLV), or PBS were intravenously injected into the tumor-bearing mice. After 24 and 48 hours, indicated tissues were isolated and weighed. DiD-specific tissue fluorescence (Abs 644 nm, Em 665 nm) was quantified for each organ using the Xenogen IVIS spectrum imaging system by the USC Imaging Core scientists blinded to the groups, and the percentage of injected dose per gram of tissue (%ID/g) was calculated.

Quantification of accumulated nanoparticles at tumor sites

SKOV3.CD19 tumors were implanted into NSG mice, as described above, and CFSE-labeled CAR-T cells (5×10^6 cells) and DiD-labeled cMLVs (1.5×10^{10} nanoparticles) were injected into tumor-bearing mice. At the indicated times, tumors were excised, fixed, frozen, cryosectioned, and mounted onto glass slides. Fluorescence of CFSE-labeled CAR-T cells and DiD-labeled cMLVs was visualized using a Zeiss 700 Confocal Laser Scanning Microscope (Inverted; Carl Zeiss). Quantification analysis was performed using Zeiss Zen microscope software.

In vivo xenograft experiments for prevention study

SKOV3.CD19 tumors were implanted into NSG mice, as described above. After tumors reached 50 to 80 mm^3, mice were randomly assigned to each treatment group: (i) PBS; (ii) CAR-T cells; (iii) CAR-T cells conjugated to empty cMLVs (CART.cMLV); (iv) a mix of CAR-T cells and cMLV(SCH; CART + cMLV(SCH)); and (v) CAR-T cells conjugated to SCH-loaded cMLVs (CART.cMLV(SCH)). Tumor growth was monitored daily and measured using calipers every 2 days. The tumor size was calculated using the formula ($width^2 \times length$)/2. Three mice from each group were sacrificed 48 hours after treatment. The tumor from each mouse was harvested for further *ex vivo* analysis. Resected tumors were minced and passed through a 70-μm nylon mesh. The single-cell suspension was washed and resuspended in PBS or TCM for further analysis.

In vivo xenograft experiments for rescue study

SKOV3.CD19 tumors were implanted into NSG mice, as described above. After the tumors were established, all the mice were injected with 3×10^6 CART.tEGFR cells. Ten days after initial adoptive CAR T-cell transfer, the mice were randomly grouped to receive the following treatments: (i) PBS; (ii) CAR-T cells; (iii) CAR-T cells conjugated to empty cMLVs (CART.cMLV); (iv) a mix of CAR-T cells and cMLV(SCH) (CART + cMLV(SCH)); and (v) CAR-T cells conjugated to SCH-loaded cMLVs (CART.cMLV (SCH)). Each mouse was injected with 2.5×10^6 CAR-positive T cells. For mice treated with unconjugated cMLVs, 10^9 drug-loaded cMLVs were coinfused with CAR-T cells. Forty-eight hours after the second adoptive T-cell transfer, the mice were sacrificed. The spleens and tumors were harvested for *ex vivo* analyses. Resected spleens were minced and passed through a 70-μm nylon mesh. Red blood cells were lysed in lysis buffer (155 mmol/L NH_4Cl, 12 mmol/L $NaHCO_3$, and 0.1 mmol/L EDTA in MilliQ water) for 10 minutes at room temperature and washed once with PBS. Splenocytes were centrifuged at $2000 \times g$ for 5 minutes at 4°C and resuspended in either PBS or TCM for further analysis.

Ex vivo analysis

Three analyses were performed on harvested tumors: (i) anti-CD3/anti-CD28–induced intracellular IFNγ cytokine staining; (ii) phospho-CREB; and (iii) Ki-67 expression in CAR-T cells. For intracellular IFNγ detection, a total of 0.5×10^6 cells were stimulated with human CD3/CD28 antibodies (2 μg/mL) and Brefeldin A (10 ng/mL). The culture was incubated for 6 hours at 37 °C in 96-well round-bottom plates and stained as described previously (36). After washing, the cells were surface stained with fluorophore-conjugated anti-human CD3, CD45, and EGFR. Cells were then permeabilized in 100 μL of cytofix/cytoperm solution (BD Bioscience) at 4°C for 10 minutes, washed with per/wash buffer (BD Bioscience), and stained with PE-conjugated anti-IFNγ at 4°C for 30 minutes.

For intracellular phospho-CREB staining, cells surface stained as stated above were fixed with 4% paraformaldehyde (PFA), followed by permeabilization in methanol for 30 minutes on ice. Cells were then stained with Alexa Fluor 488–conjugated anti-human phospho-CREB for 30 minutes at 4°C.

For Ki-67 staining, cells stained with fluorophore-conjugated anti-human CD3, CD45, and EGFR were fixed with 80% ethanol and incubated at −20°C for 48 hours. Cells were washed twice with staining buffer (PBS with 1% FBS, 0.09% NaN_3), centrifuged at $200 \times g$ for 10 minutes and resuspended to a concentration of 10^7 cells/mL. Cells were then stained with anti–Ki-67 antibody for 30 minutes at room temperature in the dark, washed twice with the staining buffer, and centrifuged at $200 \times g$ for 5 minutes. Flow cytometry analysis was carried out using the MACSQuant Instrument from Miltenyi Biotec.

Intratumoral SCH-58261 concentration measurements *ex vivo*

Using HPLC, the SCH concentration in the frozen tumor tissues was quantified as described previously (33). Briefly, thawed tumor tissues were homogenized in ethyl acetate, with a known concentration of SCH-442416 (Sigma-Aldrich) control drug, added to each sample as an internal standard. The samples were centrifuged, and the organic layer was transferred to a clean tube. The organic layer was evaporated under a stream of argon and rehydrated in diluted acetonitrile. After running the samples on HPLC, the peak heights were analyzed to determine the intratumoral SCH concentration.

Statistical analysis

Statistical analysis was performed in GraphPad Prism version 5.01. The differences between two groups were determined with the Student *t* test. The differences among three or more groups were determined with one-way analysis of variance (ANOVA) with Tukey multiple comparison. Tumor growth curves were analyzed using one-way ANOVA with repeated measures (Sidak multiple comparison method). Mice survival curves were evaluated by the Kaplan–Meier analysis (log-rank test with Bonferroni correction). A P value <0.05 was considered statistically significant. Significance of findings was defined as: ns = not significant; $P > 0.05$; *, $P < 0.05$; **, $P < 0.01$; ***, $P < 0.001$; ****, $P < 0.0001$.

Results

Nanoparticles stably attached to the surface of CAR-T cells

To improve the efficacy of CAR-engineered T-cell therapy, we used CAR-T cells as chaperones to carry nanoparticles loaded with SCH-58261. Cross-linked multilamellar liposomal vesicles (cMLV) were conjugated to the surface of CAR-T cells. According to previous reports, high levels of free thiols have been detected on the surfaces of T, B, and hematopoietic stem cells (26). Therefore, we used thiol-reactive maleimide headgroups present on the lipid bilayer surface of the cMLVs to stably couple the nanoparticles to the cell surface. The conjugation was performed in two steps. First, CAR-T cells and cMLVs containing maleimide-functionalized lipids were coincubated to permit coupling of the liposomes to free thiols on the cell surface. After the initial coupling reaction, the conjugated cells underwent *in situ* PEGylation to quench residual reactive groups on the cMLVs. To determine the maximum number of particles that could be conjugated per T cell, we performed a nanoparticle conjugation reaction at different cMLV to T-cell ratios (5,000:1, 1,000:1, 500:1, 250:1, and 100:1). At a ratio of 1000:1, the conjugation of cMLVs reached a saturation point that resulted in an average of 287 ± 49 surface-bound nanoparticles per cell (Fig. 1B; Supplementary Table S2). The average conjugation efficiency of the nanoparticles on the T-cell population was 55.9% (Fig. 1C and D). Moreover, single-cell imaging and three-dimensional reconstruction of CART.cMLVs demonstrated that the nanoparticles were distributed in several clusters on the cell surface (Fig. 1E; Supplementary Fig. S1).

CAR-T cells conjugated with nanoparticles maintain T-cell effector functions

We next sought to test whether surface-bound cMLVs could impact key cellular functions of CAR-T cells, such as cell cytokine secretion, cytotoxicity, and migration. To express CARs on T cells, activated human PBMCs were transduced with a lentiviral vector to deliver an anti-CD19 CAR consisting of CD28 and CD3ζ intracellular signaling domains. FACS analysis of surface CAR expression showed 50% transduction efficiency (Supplementary Fig. S2A). CAR-T cells with and without cMLV conjugation were cocultured with either SKOV3.CD19 or K562.CD19 target cells for 4 hours. CARTs and CART.cMLVs stimulated with SKOV3.CD19 target cells induced 17.05% ± 0.07% and 19.15% ± 1.63% $IFN\gamma^+$ T-cell populations, respectively, indicating that both CARTs and CART.cMLVs were able to secrete IFNγ with similar efficiency (Fig. 2A and B). When cMLVs were labeled with DiD dye, IFNγ was secreted from both cells with and without surface-conjugated cMLVs (Supplementary Fig. S2B). Surface conjugation of cMLVs did not reduce CAR T-cell cytotoxicity against SKOV3.CD19 or

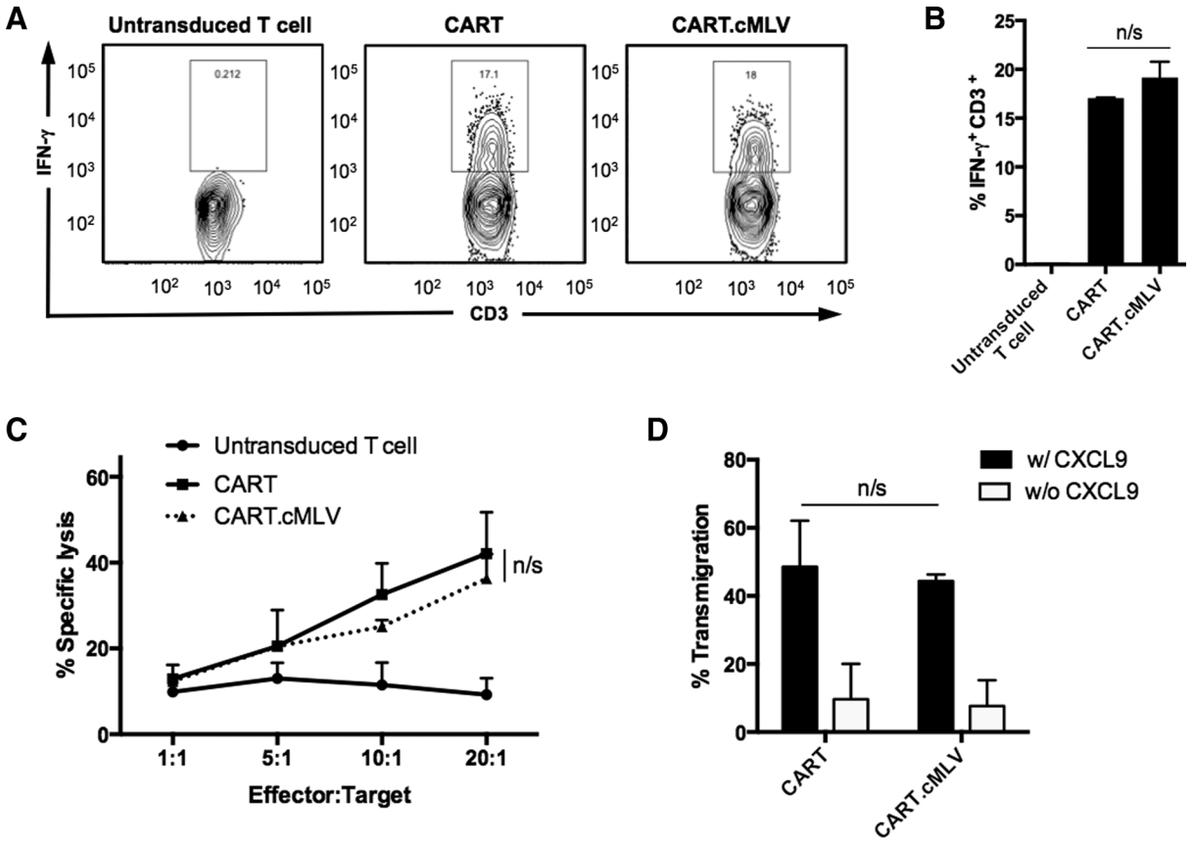

Figure 2.

Conjugation of cMLV does not alter CAR T-cell function. **A,** Representative flow cytometry analysis of untransduced T cells or CAR-T cells, either unconjugated (CART) or conjugated with empty cMLVs (CART.cMLV), stimulated with SKOV3.CD19 cells for 6 hours to detect IFNγ release. Untransduced CAR-T cells served as a negative control. IFNγ was measured with intracellular staining. **B,** Bar graph of summarized statistics of triplicates for intracellular IFNγ. **C,** *In vitro* cell cytotoxicity assay. CART or CART.cMLV were cocultured with SKOV3.CD19 cells for 4 hours, and cytotoxicity was measured. Untransduced CAR-T cells served as a negative control. $n = 3$ samples per group; mean ± SD; n/s: not significant; *, $P < 0.05$; **, $P < 0.01$; ***, $P < 0.001$, one-way ANOVA with Tukey multiple comparison. **D,** Transmigration assay. CARTs or cMLVs (10^6) conjugated CAR-T cells (CART.cMLV) were seeded in the upper chambers of a transwell with or without addition of the chemoattractant CXCL9 to the lower chambers. After 6 hours of incubation, media from the lower chambers were collected and CAR-T cells were counted. All data are representative of three independent experiments. Summarized statistics are displayed in the graphs. $n = 3$ samples per group, mean ± SD; n/s: not significant; *, $P < 0.05$; **, $P < 0.01$; ***, $P < 0.001$, one-way ANOVA with Tukey multiple comparison.

K562.CD19 cells (Fig. 2C; Supplementary Fig. S2C). We then assessed CAR T-cell transmigration capabilities *in vitro*. Comparable percentages of conjugated and unconjugated cells migrated to the lower chamber of the transwell coculture system, indicating that CART.cMLV cells maintain their transmigration capabilities (Fig. 2D). Thus, the cell surface conjugation of cMLVs does not hinder recognition of target cells, IFNγ secretion, cell cytotoxicity, or migration.

Conjugated CAR-T cells increase tumor localization and systemic circulation of cMLVs

In vitro, we demonstrated that cMLV nanoparticles could be stably conjugated to the CAR T–cell surface while maintaining its ability to release loaded drug in a sustained manner and did not disrupt CAR T-cell effector functions (Supplementary Fig. S2D). To determine whether conjugation of cMLVs to CAR-T cells could improve the accumulation of nanoparticles to the tumor site, we performed an *in vivo* biodistribution study. DiD-labeled cMLVs alone (cMLV(DiD)), mixed with CAR-T cells (CART + cMLV (DiD)), or conjugated to CAR-T cells (CART.cMLV(DiD)) were intravenously injected into NSG mice bearing SKOV3.CD19 tumors, and DiD-tagged cMLV accumulation was monitored in different organs. At 24 hours, significantly higher cMLV accumulation was detected from CART.cMLV(DiD) in the tumors ($P < 0.001$), spleens ($P < 0.001$), lymph nodes ($P < 0.01$), and lungs ($P < 0.01$) compared with cMLV and CART + cMLV groups. No significant difference in cMLV accumulation was noted between cMLV(DiD) and CART + cMLV(DiD) groups in any tissues, and no significant difference in DiD signal was detected at 24 hours in circulating blood in any group (Fig. 3A and B). At 48 hours, the CART.cMLV(DiD) group demonstrated higher cMLV accumulation in the blood ($P < 0.05$), tumors ($P < 0.05$), spleens ($P < 0.05$), and lungs ($P < 0.05$) compared with both cMLV(DiD) and CART + cMLV (DiD) groups (Fig. 3C and D). CAR T-cell conjugation to cMLVs resulted in significantly lower cMLV accumulation in the liver compared with both cMLV(DiD) and CART + cMLV(DiD) groups at 24 ($P < 0.05$) and 48 ($P < 0.001$) hours.

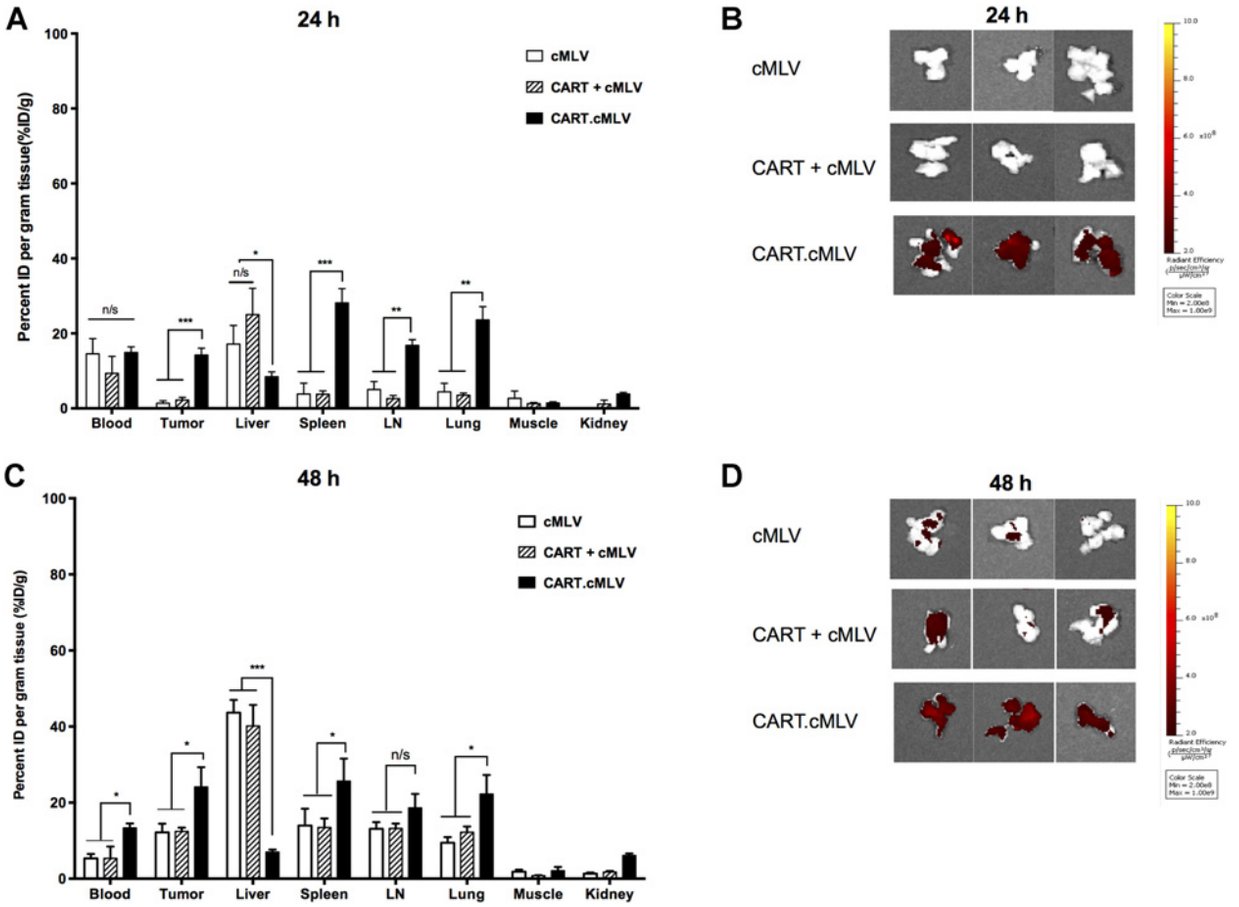

Figure 3.

cMLVs bound to CAR T cells show more efficient infiltration to antigen-expressing tumors than free cMLVs. NSG mice ($n = 3$ mice per group) bearing subcutaneous SKOV3.CD19 tumors were intravenously injected with 5×10^6 conjugated CAR-T cells (CART.cMLV), coinfused with DiD-labeled cMLVs (CART+cMLV), or an equivalent number of DiD-labeled cMLVs alone (cMLV). **A** and **B,** After 24 hours and (**C, D**) 48 hours, indicated tissues were isolated and dissected. **A** and **C,** Specific DiD fluorescence for each tissue specimen was quantified using the IVIS spectrum imaging system, and the mean percentage of injected dose per gram of tissue (% ID/g) was calculated. **B** and **D,** Representative images of DiD fluorescence from the tumor tissues. All data are representative of three independent experiments. Summarized statistics are displayed in the graphs. $n = 3$ mice per group; mean ± SD; n/s: not significant; *, $P < 0.05$; **, $P < 0.01$; ***, $P < 0.001$, one-way ANOVA with Tukey multiple comparison.

Surface-conjugated cMLVs colocalize with CAR-T cells inside the tumor mass

We next evaluated the tumor infiltration properties of carrier CAR-T cells by confocal imaging of histologic SKOV3.CD19 tumor sections that had been treated with cMLV-conjugated, or unconjugated, fluorescent-labeled CAR-T cells. Representative confocal images demonstrate that the surface conjugation of cMLVs does not impede intratumoral CAR T-cell migration (Fig. 4A and B). Both CART.cMLV and CART + cMLV groups had comparable infiltration of T cells (Fig. 4C). The density of CAR-T cells in the CART.cMLV- and CART + cMLV–treated tumors was 0.26 ± 0.1 cells/mm^2 and 0.35 ± 0.2 cells/mm^2, respectively. However, the colocalization of CAR-T cells and cMLVs was only observed inside tumors treated with CART.cMLVs. The percentage of colocalization was 78.57% ± 26.7% in the CART.cMLV–treated tumors compared with no detection in CART + cMLV–treated tumors (Fig. 4D). These results indicate that cMLV conjugation to the CAR-T cells is able to increase the amount of cMLVs delivered to the tumor without impeding the migration of T cells.

Codelivery of CAR-T cells with A2aR antagonist improves antitumor responses *in vivo*

To test whether the pharmacologic inhibition of A2aR could prevent CAR T-cell hypofunction in the adenosine-rich TME, we monitored tumor growth and intratumoral CAR T-cell infiltration *in vivo*. SKOV3.CD19 tumor–bearing mice were assigned into six different groups as shown in Fig. 5A. Animals in all treatment groups showed tumor progression. CART, CART.cMLV, CART + cMLV(SCH), and CART.cMLV(SCH) treatment groups showed statistically significant tumor growth control, from day 2 until day 17 after treatment, when compared with the PBS treatment group (Fig. 5B; Supplementary Table S3). Compared with other treatment groups, CART.cMLV(SCH) treatment demonstrated the most distinguished tumor growth inhibition, resulting in significantly smaller tumors for all days measured post ACT (Fig. 5B). Consequently, CART.cMLV(SCH) treatment improved the survival of the mice compared with CART ($P < 0.0001$, log-rank test), CART.cMLV ($P < 0.0001$, log-rank test), and CART + cMLV(SCH; $P = 0.0008$, log-rank test) treatment groups. CART, CART.cMLV,

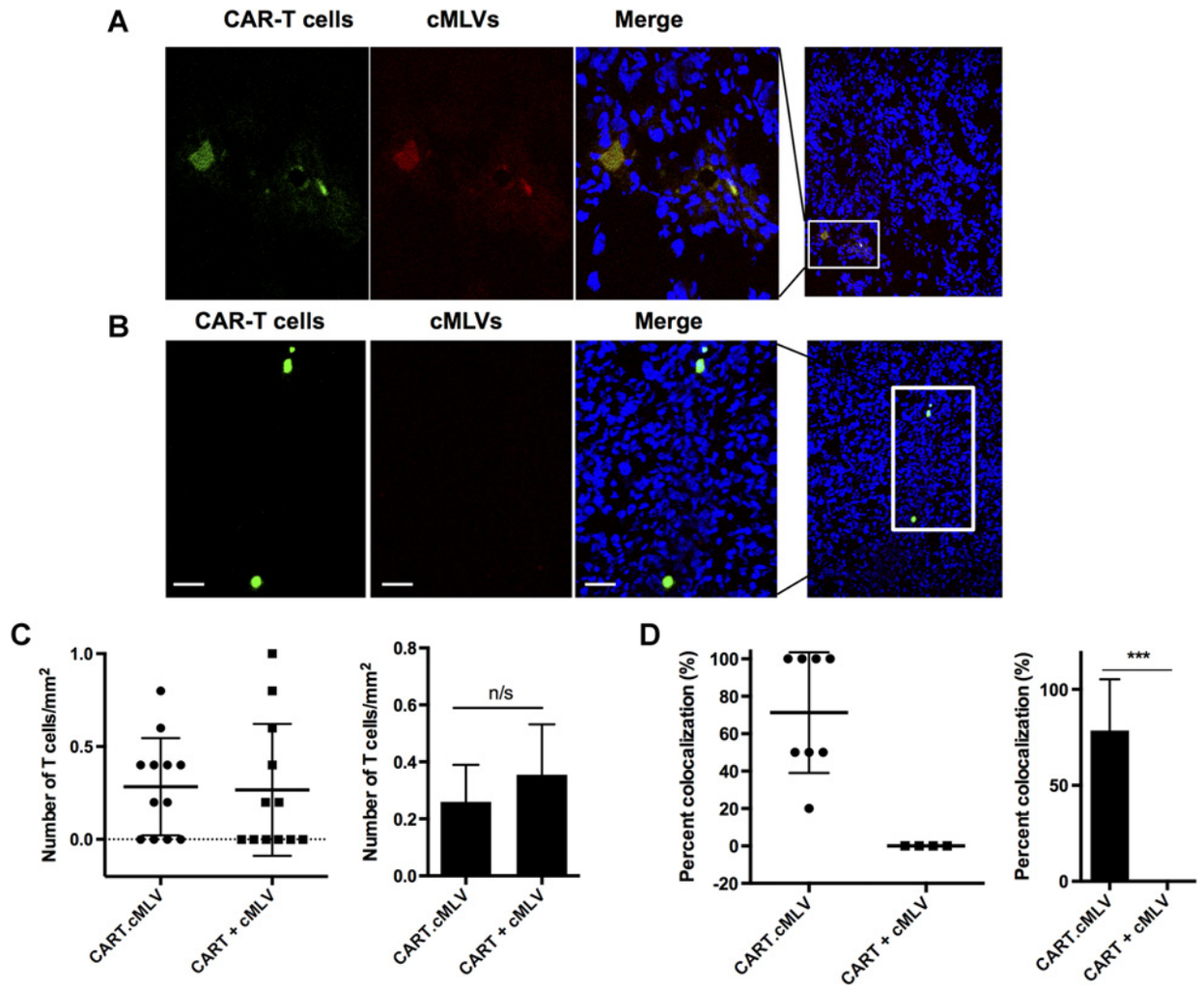

Figure 4.

Surface-conjugated cMLVs colocalize with CAR-T cells inside the tumor mass 48 hours after CAR T-cell infusion. **A,** Representative confocal images of DiD-labeled cMLV- (red) conjugated CAR-T cells (green) infiltrating an SKOV3.CD19 tumor 48 hours after injection (CART.cMLV). **B,** Representative confocal images of coadministered DiD-labeled cMLVs (red) and CAR-T cells (green) without conjugation infiltrating an SKOV3.CD19 tumor 48 hours after infusion (CART + cMLV). Scale bar: 30 μm. **C,** Density of SKOV3.CD19 tumor-infiltrating CAR-T cells from either the CART.cMLV or CART + cMLV group. **D,** Percentage of tumor-infiltrating CAR-T cells that were colocalized with cMLVs inside the tumor tissues. Summarized statistics are displayed in the graphs. $n = 6$ mice per group; mean ± SD; n/s: not significant; *, $P < 0.05$; **, $P < 0.01$; ***, $P < 0.001$, one-way ANOVA with Tukey multiple comparison.

CART + cMLV(SCH), and CART.cMLV(SCH) had a median survival of 22, 22, 24, and 36 days after treatment, respectively. Both PBS and cMLV treatment had median survival of 22 days. Only CART.cMLV(SCH) treatment significantly improved the median survival compared with PBS and cMLV groups ($P = 0.0003$ for PBS and $P = 0.0002$ for cMLV, log-rank test; Fig. 5C).

To explore how SCH affected tumor-infiltrating T cells, we analyzed T-cell engraftment and functionality. $CD3^+$ and $CD45^+$ T-cell engraftment in the tumor was evaluated on day 2 after treatment. CART.cMLV(SCH) had higher T-cell engraftment (52.96% ± 15.5%) compared with CART (15.06 ± 1.2%, $P = 0.0134$), CART.cMLV (15.36% ± 1.9%, $P = 0.0139$), and CART + cMLV(SCH; 16.93% ± 0.6%, $P = 0.0157$) treatment groups (Fig. 5D). We also evaluated the functionality of tumor-infiltrating T cells that were exposed to the adenosine-rich immunosuppressive TME *in vivo*. The CART.cMLV(SCH) treatment group showed significantly higher intracellular IFNγ expression (MFI = 744.24 ± 45.3) in $CD45^+$ T cells compared with CART (MFI = 335.8 ± 91.2, $P = 0.0023$), CART.cMLV (MFI = 307.57 ± 53.6, $P = 0.0004$), and CART + cMLV(SCH; 611.52 ± 26.21, $P = 0.0118$) treatment groups. The free cMLV(SCH) treatment group, CART + cMLV(SCH), also resulted in an increased IFNγ expression compared with CART ($P = 0.0073$) and CART.cMLV ($P = 0.0009$) treatments, although this level was less than that observed with CART.cMLV(SCH) treatment (Fig. 5E).

To determine if the functional preservation of tumor-infiltrating T cells is, at least in part, the result of A2a receptor blockade, we tested phosphorylated CREB downstream of A2aR in T cells. Our data showed that $CD45^+$ T cells from the CART- and CART.cMLV–treated groups had significantly higher phosphorylated CREB

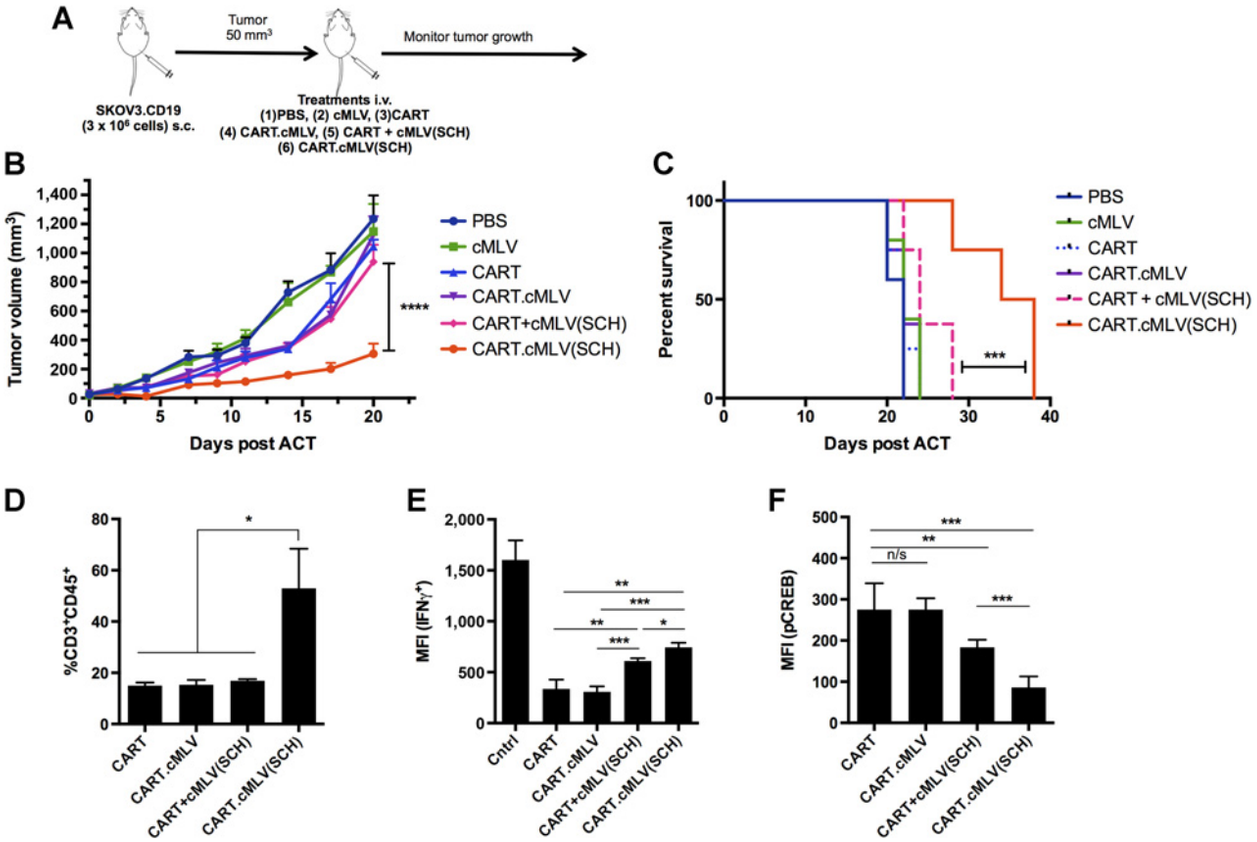

Figure 5.

Anti-CD19 CAR-T cells conjugated with SCH-58261–releasing cMLVs were prevented from developing hypofunction in SKOV3.CD19 tumors. SKOV3.CD19 cells (3×10^6) were injected subcutaneously into the right flank of NSG mice. Mice were randomized into six groups and treated with indicated treatments via i.v. injections. **A,** Schematic illustration of targeted *in vivo* delivery of different treatments. **B,** Tumor size was measured with a digital caliper. $n = 8$ mice per group; mean ± SD; n/s, not significant; *, $P < 0.05$; **, $P < 0.01$; ***, $P < 0.001$; ****, $P < 0.0001$, one-way ANOVA with repeated measures (Sidak multiple comparison method). **C,** Mouse survival curves for the different treatment groups were calculated using the Kaplan–Meier method. **D–F,** After indicated treatments, flank tumors were harvested and digested for *ex vivo* analyses. The quantity and function of tumor-infiltrating CAR-T cells were evaluated. **D,** Percentage of $CD3^+CD45^+$ T cells in the tumor at day 2 after treatment. **E,** Intracellular IFNγ secretion of tumor-infiltrating T cells upon *ex vivo* stimulation with anti-hCD3 and anti-hCD28 (2 μg/mL of each) day 2 after treatments. **F,** Phosphorylated CREB (pCREB) expression tumor-infiltrating T cells day 2 after treatments. All data are representative of two independent experiments. Summarized statistics are displayed in the graphs. $n = 3$ mice per group; mean ± SD; n/s: not significant; *, $P < 0.05$; **, $P < 0.01$; ***, $P < 0.001$; ****, $P < 0.0001$, one-way ANOVA with Tukey multiple comparison.

compared with T cells harvested from the CART + cMLV(SCH) and CART.cMLV(SCH)–treated groups, indicating that SCH released from surface-engineered CAR-T cells could block A2a receptor signaling mediated by adenosine in TME. CART.cMLV (SCH) treatment resulted in lower phosphorylated CREB compared with CART + cMLV(SCH; $P < 0.0001$; Fig. 5F). Overall, compared with free cMLV(SCH) treatment, conjugation of cMLV (SCH) to CAR-T cells significantly prolonged tumor growth inhibition, indicating higher efficiency in blocking the A2a receptor pathway and preventing CAR T-cell hypofunction.

Codelivery of CAR-T cells and A2aR antagonist reversed T-cell hypofunction

Although tumor-infiltrated CAR-T cells can migrate into the tumor mass, they tend to gradually lose tumor killing and inflammatory cytokine secretion abilities after entering the adenosine-rich TME (11, 17, 37). We hypothesized that hypofunctional tumor-residing T cells could regain their effector functions upon the blocking of A2aR signaling with SCH. To demonstrate the potential of our conjugated system in this application, we established an *in vivo* model with hypofunctional tumor-residing CAR-T cells in the TME by an initial intravenous infusion of CD19 CAR-T cells that express a truncated epidermal growth factor receptor (tEGFR) to the tumor-bearing mice (Supplementary Fig. S3A) These CAR-T cells are designated as CART.tEGFR. The EGFR surface marker was used to trace the initial population of hypofunctional tumor-residing CAR-T cells, enabling us to distinguish them from the subsequent treatment dose of surface-engineered CAR-T cells lacking EGFR. Ten days after the initial CART.tEGFR cell transfer, the rescue treatment was infused to mice in five different groups (Fig. 6A).

Two days after the treatments, 5 of 6 tumor-bearing mice that received CART.cMLV(SCH) treatment showed over 50% reduction in tumor size, with 1 mouse showing 44% reduction. The combination treatment group of CART + cMLV(SCH) showed more than 25% reduction in tumor size in 2 of 6 mice. Tumor-

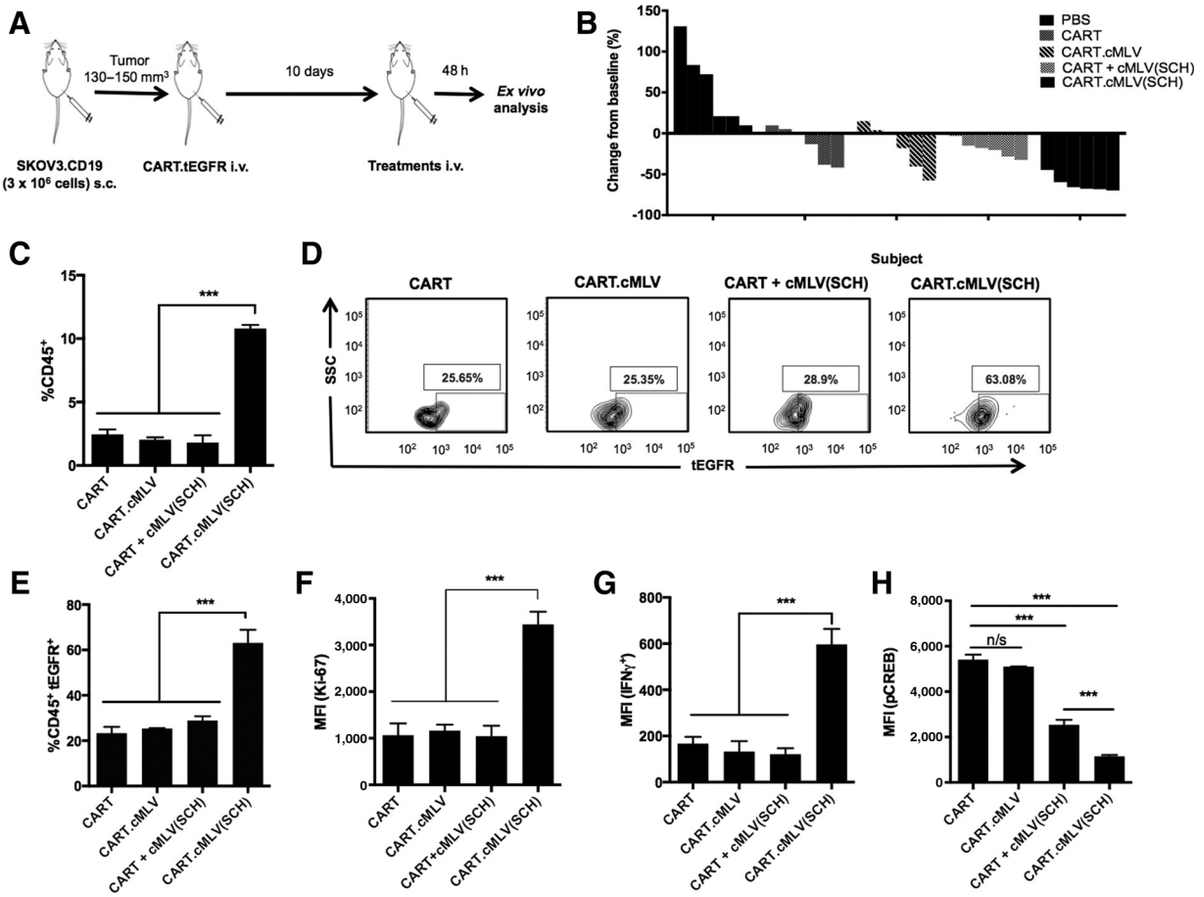

Figure 6.

Anti-CD19 CAR-T cells conjugated with SCH-58261–releasing cMLVs were able to rescue hypofunctional tumor-infiltrating T cells in SKOV3.CD19 tumors. **A,** Schematic illustration of targeted *in vivo* delivery of CART.tEGFR cells followed by treatment with CAR-T cells conjugated with SCH-loaded and unloaded cMLVs 10 days later to assess rescue. **B,** The waterfall plot displaying the percentage change in the tumor size from baseline at day 35 post i.v. injections. $n = 6$ mice per group; mean ± SD; n/s: not significant; *, $P < 0.05$; **, $P < 0.01$; ***, $P < 0.001$, one-way ANOVA with Tukey multiple comparison. **C,** The percentage of $CD45^+$ T cells in the tumor 2 days after treatments. **D,** Representative FACS plots of the percentage of CART.tEGFR cells in the tumor 2 days after treatment. **E,** Quantitative graph showing the percentage of CART.tEGFR cells in the tumor 2 days after indicated treatments. **F,** Ki-67 expression in CART.tEGFR cells 2 days after treatments. **G,** Intracellular IFNγ in tumor-infiltrating CART.tEGFR cells upon *ex vivo* stimulation with anti-hCD3 and anti-hCD28 (2 μg/mL of each) 2 days after treatments. **H,** Phosphorylated CREB (pCREB) expression in CART.tEGFR cells 2 days after treatments. All data are representative of two independent experiments. Summarized statistics are displayed in the graphs. $n = 3$ mice per group; mean ± SD; n/s: not significant; *, $P < 0.05$; **, $P < 0.01$; ***, $P < 0.001$, one-way ANOVA with Tukey multiple comparison.

bearing mice that received either CART or CART.cMLV had no significant reduction in tumor size, and the tumor-bearing mice that received PBS treatment showed an overall increase in tumor size (Fig. 6B; Supplementary Fig. S3B and S3C). Tumor-infiltrating T cells, including CAR-positive cells, were isolated from tumors for further *ex vivo* analysis. As shown in Fig. 6C, CART.cMLV(SCH) treatment resulted in 10.79% ± 0.3% total T-cell population, which is significantly higher than all other treatment groups: CART ($P < 0.001$), CART.cMLV ($P < 0.001$), and CART + cMLV(SCH; $P < 0.001$; Fig. 6C).

We further investigated the effect of these treatments on the initial hypofunctional CART.tEGFR cells. Tumors treated with CART, CART.cMLV, and CART + cMLV(SCH) had 25.65% ± 2.8%, 25.35% ± 0.5%, and 28.90% ± 3.1% intratumoral CART.tEGFR, respectively, whereas CART.cMLV(SCH)–treated tumors had 63.08% ± 5.8% CART.tEGFR cells, significantly higher than all other groups ($P < 0.001$; Fig. 6D and E). The proliferation of CAR-T cells was assessed by the expression of Ki-67. CART.cMLV(SCH) showed significantly higher Ki-67 expression (MFI = 3442.4 ± 272.3) compared with other treatment groups: CART (MFI = 1066.1 ± 253.5, $P = 0.0004$), CART.cMLV (MFI = 1162.5 ± 129.5, $P = 0.0002$), and CART + cMLV(SCH; MFI = 1044.32 ± 224.8, $P = 0.0003$; Fig. 6F).

Next, we evaluated the ability of this CART-chaperoned drug to restore inflammatory function of the hypofunctional CART.tEGFR population. The CART.cMLV(SCH) treatment group showed significantly higher IFNγ secretion in CART.tEGFR cells than that of CART, CART.cMLV, or CART+cMLV(SCH) groups ($P < 0.001$; Fig. 6G). Evaluation of phosphorylated-CREB (pCREB) expression in CART.tEGFR cells showed that the CART.cMLV(SCH) treatment significantly reduced pCREB in CART.tEGFR cell populations compared with the CART,

CART.cMLV, and CART+cMLV(SCH) treatment groups ($P < 0.001$; Fig. 6H). Using HPLC, we quantified the intratumoral SCH concentrations in mice treated with SCH, including the groups CART + cMLV(SCH) and CART.cMLV(SCH). The conjugated group had significantly higher SCH accumulation within the tumor tissue compared with the unconjugated group (Supplementary Fig. S3D). We also confirmed that SKOV3.CD19 cells were not directly affected by SCH (Supplementary Fig. S3E), indicating that SKOV3.CD19 tumor reduction was mainly achieved by the effect of SCH on the tumor-infiltrating CAR-T cells. Taken together, this collective evidence suggests that the surface-engineered CART system can effectively deliver a small-molecule inhibitor of A2aR to TME, thereby rescuing hypofunctional tumor-residing T cells *in vivo*.

Discussion

Our strategy to enhance CAR T-cell efficacy in solid tumors was to conjugate nanoparticles loaded with a small-molecule inhibitor of the A2a receptor pathway onto the surface of CAR-T cells. Ohta and colleagues demonstrated that a variety of adenosine receptor blockades, including antagonists such as caffeine and ZM241385, which selectively target both A2aR and A2bR, improved tumor growth suppression, reduced metastasis, and prevented neovascularization by antitumor T cells (12). This comprehensive study suggests that the A2aR pathway is a promising immunotherapeutic target to prevent inhibition of T-cell function in the TME of aggressive cancers that produce adenosine. Although other methods to block the A2aR pathway exist, such as genetically engineering CAR-T cells with the CRISPR/Cas system or receptor siRNA knockdown, the major advantage of this strategy is the ability of the drug to affect endogenous T cells and circulating CAR-T cells, as well as the carrier CAR-T cells themselves. These findings corroborate previous results reported by Stephan and colleagues and Huang and colleagues (25, 26), which demonstrated that liposomal nanoparticles with thiol-reactive maleimide headgroups could be successfully conjugated to the thiol-rich surface of T cells, and that this could be done without altering effector functions and transmigration capabilities of the T cells.

Our biodistribution study further showed that CAR-T cells enhanced the efficacy of therapeutic drugs by actively directing drug-loaded nanoparticles to the tumor site *in vivo* (38, 39), an event driven by the ability of CAR-T cells to migrate into the tumor mass through tumor-associated chemokine attraction. Overall, CART.cMLVS(DiD) had the highest particle accumulation at the tumor site, reemphasizing the importance of cell-mediated delivery. Both cMLV(DiD) and CART + cMLV(DiD) resulted in significantly higher cMLV accumulation in the liver, which is where liposomal nanoparticles are typically cleared from the system by Kupffer and endothelial cells (40, 41). However, although CART.cMLV(DiD) showed significantly lower cMLV accumulation in the liver, increased accumulation was observed in lymphoid tissues, such as the lymph nodes, spleen, and lungs. These data provide evidence that CAR-T cell–bound nanoparticles may be retained in circulation for a longer period of time than free nanoparticles, owing to reduced nanoparticle clearance by the liver.

In order to achieve maximal drug action on hypofunctional T cells within the TME, the drug-loaded nanoparticles must be able to reach the immune cells deep within the tumor mass. In this regard, the CART.cMLV drug-delivery system promotes the colocalization of nanoparticles and CAR-T cells inside the tumor mass due to the innate mobility of T cells within the tumor to deliver drugs inside the TME (27, 42). Confocal microscopic images showed that cMLVs from the CART.cMLV group were able to penetrate deep inside the tumor and colocalize with CAR-T cells. HPLC analysis of the tumor tissue after treatment with CART.cMLV(SCH) also showed higher concentration of SCH-58261 compared with delivery with free cMLV(SCH). This maximum intratumoral localization of cMLVs increased drug release into the TME, which could be a major factor contributing to the higher potency of CART.cMLV(SCH) therapy.

The tumor-targeted CART.cMLV(SCH) therapeutic system was effective at preventing hypofunction of nanoparticle-conjugated CAR-T cells. Groups treated with CART.cMLV(SCH) demonstrated significant tumor growth suppression compared with groups without the conjugated drug. Prophylactic CART.cMLV(SCH) treatment showed high tumor engraftment of T cells with low CREB phosphorylation, indicating the mechanistic importance of A2aR blockade that leads to increased T-cell proliferation (15). This is supported by our observation that CART.cMLV(SCH) had a higher percentage of tumor-infiltrated T cells and increased IFNγ production compared with the other groups (12, 14). It should be noted, however, that the maximal IFNγ secretion in our most successful treatment group was still significantly lower than the control T cells isolated from tumor-free mice, suggesting that in addition to A2aR signaling, CAR-T cells could be exposed to other mechanisms for immunosuppression in this SKOV3 tumor model.

We further aimed to restore activity to hypofunctional CAR-T cells. This rescue treatment mirrors a clinical setting where patients have preexisting TILs or have previously received CAR T-cell therapy. CART.cMLV(SCH) treatment resulted in significantly higher IFNγ secretion in the initial hypofunctional CART.tEGFR cell population upon *ex vivo* restimulation compared with other treatment groups. In the CART.cMLV(SCH) treatment group, the CART.tEGFR population also showed lower phosphorylated CREB and significantly higher cell number compared with other groups, presumably due to the release of A2aR-mediated inhibition of T-cell proliferation (15). The immediate reduction of tumor burden after CART.cMLV(SCH) treatment is most likely caused by the recovery of cytotoxicity induced by the CART.tEGFR cell population. This is supported by the fact (i) CART.cMLV(SCH) treatment alone at the same dosage in our prophylactic study could only suppress, but not reduce, tumor growth; and (ii) tumor size reduction mediated by immediately infused T cells took 5 to 6 days (42), which was longer than the 2 days we observed in this study.

Although CART.cMLV(SCH) has shown promising results, further improvements and modifications could be made to expand this treatment to different clinical settings. This delivery platform is flexible, and it can be applied to other drugs, cytokines, antibodies, or any combination thereof. For example, a previous study by Stephan and colleagues successfully demonstrated that the use of different therapeutic cells, such as tumor-specific T lymphocytes and hematopoietic stem cells (HSC) as targeted delivery vehicles, increased the therapeutic efficacy of cytokines and a small-molecule inhibitor (26). Immune regulatory drugs could also be delivered in combination with immune checkpoint blockade, such as anti–PD-1, to further promote antitumor immunity (14, 19). In a previous review by Iwai and colleagues, multiple clinical studies involving anti–PD-1 and anti–PD-L1

when combined with small-molecule inhibitors of VEGF and EGFR have shown potential for the treatment of ovarian and lung cancers (43). To overcome the limitations of CAR T-cell therapy, such as the lengthy manufacturing process and toxicities due to cytokine release syndrome or on target/off tumor recognition (44), CAR-T cells could also be exchanged for other "chaperone" cells, such as natural killer (NK) cells, which can be used more universally (45).

This method of combining CAR T-cell immunotherapy with A2aR small-molecule antagonists could also be applied to various types of cancers, such as breast, prostate, brain cancers, and leukemia. These cancers have been reported to express CD73, which is associated with poor prognosis (46, 47). In this study, we selected SKOV3 as a proof-of-concept tumor model because it expresses high CD39 and CD73. SKOV3 was reported to produce a high amount of adenosine (1.1–1.7 μmol/L), and various levels of adenosine were also measured from several other human tumor models, including lung (A549: 0.56 ± 0.17 μmol/L), colon (T-84: 0.48 ± 0.02 μmol/L; TH-29: 0.47 ± 0.04 μmol/L; refs. 48, 49). Hence, further studies on tumor models other than SKOV3 are needed in order to assess the feasibility and efficacy of this immunotherapy method for treating cancer in general. Our current work is concentrated on the antitumor effects of CAR-T cells targeting a single tumor antigen (CD19). Future research using CAR-T cells that target various solid tumor antigens and *in vivo* studies in immunocompetent mouse models would provide insightful information on the significance of this delivery strategy for enhancing CAR T-cell therapy *in vivo*.

Cell-mediated drug delivery by surface engineering of CAR-T cells with nanoparticles not only enables controlled drug effects on the carrier cells, but also allows active targeting to the tissue of interest. By using CAR-T cells as chaperones, we were able to efficiently localize nanoparticles in specific tissues favorable for T-cell homing, including tumor, spleen, lungs, and lymph nodes (50). Overall, this is a promising platform that can potentially improve the efficacy and specificity of solid tumor therapies.

Disclosure of Potential Conflicts of Interest

P. Wang has ownership interest (including patents) in HRAIN Biotechnology. No potential conflicts of interest were disclosed by the other authors.

Authors' Contributions

Conception and design: N. Siriwon, Y.J. Kim, P. Wang
Development of methodology: N. Siriwon, Y.J. Kim, Y. Liu, P. Wang
Acquisition of data (provided animals, acquired and managed patients, provided facilities, etc.): N. Siriwon, Y.J. Kim, E. Siegler, X. Chen, J.A. Rohrs
Analysis and interpretation of data (e.g., statistical analysis, biostatistics, computational analysis): N. Siriwon, Y.J. Kim, P. Wang
Writing, review, and/or revision of the manuscript: N. Siriwon, Y.J. Kim, E. Siegler, J.A. Rohrs, Y. Liu, P. Wang
Administrative, technical, or material support (i.e., reporting or organizing data, constructing databases): N. Siriwon, Y.J. Kim
Study supervision: P. Wang

Acknowledgments

The authors thank Dr. Wolfgang Uckert at Humboldt University of Berlin, Germany for providing retroviral plasmid MP71. This work was supported by NIH grants (R01AI068978, R01CA170820, R01EB017206, and P01CA132681) and a translational acceleration grant from the Joint Center for Translational Medicine. We also want to thank the University of Southern California Flow Cytometry Core for assistance.

The costs of publication of this article were defrayed in part by the payment of page charges. This article must therefore be hereby marked *advertisement* in accordance with 18 U.S.C. Section 1734 solely to indicate this fact.

Received September 8, 2017; revised February 12, 2018; accepted April 26, 2018; published first May 2, 2018.

References

1. Davila ML, Riviere I, Wang X, Bartido S, Park J, Curran K, et al. Efficacy and toxicity management of 19-28z CAR T cell therapy in B cell acute lymphoblastic leukemia. Sci Transl Med 2014;6:224ra25.
2. Lee DW, Kochenderfer JN, Stetler-Stevenson M, Cui YK, Delbrook C, Feldman SA, et al. T cells expressing CD19 chimeric antigen receptors for acute lymphoblastic leukaemia in children and young adults: a phase 1 dose-escalation trial. Lancet 2015;385:517–28.
3. Brentjens RJ, Davila ML, Riviere I, Park J, Wang X, Cowell LG, et al. CD19-targeted T cells rapidly induce molecular remissions in adults with chemotherapy-refractory acute lymphoblastic leukemia. Sci Transl Med 2013;5:177ra38.
4. Morgan RA, Yang JC, Kitano M, Dudley ME, Laurencot CM, Rosenberg SA. Case report of a serious adverse event following the administration of T cells transduced with a chimeric antigen receptor recognizing ERBB2. Mol Ther 2010;18:843–51.
5. Fesnak AD, June CH, Levine BL. Engineered T cells: the promise and challenges of cancer immunotherapy. Nat Rev Cancer 2016;16:566–81.
6. Morgan RA, Dudley ME, Wunderlich JR, Hughes MS, Yang JC, Sherry RM, et al. Cancer regression in patients after transfer of genetically engineered lymphocytes. Science 2006;314:126–9.
7. Newick K, Moon EK, Albelda SM. Chimeric antigen receptor T-cell therapy for solid tumors. Mol Ther Oncolytics 2016;3:16006.
8. Quail DF, Joyce JA. Microenvironmental regulation of tumor progression and metastasis. Nat Med 2013;19:1423–37.
9. Dudley ME, Wunderlich JR, Robbins PF, Yang JC, Hwu P, Schwartzentruber DJ, et al. Cancer regression and autoimmunity in patients after clonal repopulation with antitumor lymphocytes. Science 2002;298:850–4.
10. Louis CU, Savoldo B, Dotti G, Pule M, Yvon E, Myers GD, et al. Antitumor activity and long-term fate of chimeric antigen receptor-positive T cells in patients with neuroblastoma. Blood 2011;118:6050–6.
11. Jiang Y, Li Y, Zhu B. T-cell exhaustion in the tumor microenvironment. Cell Death Dis 2015;6:e1792.
12. Ohta A, Gorelik E, Prasad SJ, Ronchese F, Lukashev D, Wong MK, et al. A2A adenosine receptor protects tumors from antitumor T cells. Proc Natl Acad Sci U S A 2006;103:13132–7.
13. Cekic C, Linden J. Adenosine A2A receptors intrinsically regulate CD8+ T cells in the tumor microenvironment. Cancer Res 2014;74:7239–49.
14. Beavis PA, Henderson MA, Giuffrida L, Mills JK, Sek K, Cross RS, et al. Targeting the adenosine 2A receptor enhances chimeric antigen receptor T cell efficacy. J Clin Invest 2017;127:929–41.
15. Jin D, Fan J, Wang L, Thompson LF, Liu A, Daniel BJ, et al. CD73 on tumor cells impairs antitumor T-cell responses: a novel mechanism of tumor-induced immune suppression. Cancer Res 2010;70:2245–55.
16. Lappas CM, Rieger JM, Linden J. A2A adenosine receptor induction inhibits IFN-gamma production in murine CD4+ T cells. J Immunol 2005;174:1073–80.
17. Stagg J, Smyth MJ. Extracellular adenosine triphosphate and adenosine in cancer. Oncogene 2010;29:5346–58.
18. Bono MR, Fernández D, Flores-Santibáñez F, Rosemblatt M, Sauma D. CD73 and CD39 ectonucleotidases in T cell differentiation: Beyond immunosuppression. FEBS Lett 2015;589:3454–60.

19. Beavis PA, Divisekera U, Paget C, Chow MT, John LB, Devaud C, et al. Blockade of A2A receptors potently suppresses the metastasis of CD73+ tumors. Proc Natl Acad Sci USA 2013;110:14711–6.
20. Fredholm BB, IJzerman AP, Jacobson KA, Klotz KN, Linden J. International Union of Pharmacology. XXV. Nomenclature and classification of adenosine receptors. Pharmacol Rev 2001;53:527–52.
21. Cacciari B, Pastorin G, Spalluto G. Medicinal chemistry of A2A adenosine receptor antagonists. Curr Top Med Chem 2003;3:403–11.
22. Bae YH, Park K. Targeted drug delivery to tumors: Myths, reality and possibility. J Control Release 2011;153:198–205.
23. Nishida N, Yano H, Nishida T, Kamura T, Kojiro M. Angiogenesis in cancer. Vasc Health Risk Manag 2006;2:213–19.
24. Byrne JD, Betancourt T, Brannon-Peppas L. Active targeting schemes for nanoparticle systems in cancer therapeutics. Adv Drug Deliv Rev 2008;60:1615–26.
25. Huang B, Abraham WD, Zheng Y, Bustamante López SC, Luo SS, Irvine DJ. Active targeting of chemotherapy to disseminated tumors using nanoparticle-carrying T cells. Sci Transl Med 2015;7:291ra94.
26. Stephan MT, Moon JJ, Um SH, Bershteyn A, Irvine DJ. Therapeutic cell engineering with surface-conjugated synthetic nanoparticles. Nat Med 2010;16:1035–41.
27. Mrass P, Takano H, Ng LG, Daxini S, Lasaro MO, Iparraguirre A, et al. Random migration precedes stable target cell interactions of tumor-infiltrating T cells. J Exp Med 2006;203:2749–61.
28. Dai B, Xiao L, Bryson PD, Fang J, Wang P. PD-1/PD-L1 blockade can enhance HIV-1 Gag-specific T cell immunity elicited by dendritic cell-directed lentiviral vaccines. Mol Ther 2012;20:1800–9.
29. Milone MC, Fish JD, Carpenito C, Carroll RG, Binder GK, Teachey D, et al. Chimeric receptors containing CD137 signal transduction domains mediate enhanced survival of T cells and increased antileukemic efficacy in vivo. Mol Ther 2009;17:1453–64.
30. Engels B, Cam H, Schüler T, Indraccolo S, Gladow M, Baum C, et al. Retroviral vectors for high-level transgene expression in T lymphocytes. Hum Gene Ther 2003;14:1155–68.
31. Han X, Bryson PD, Zhao Y, Cinay GE, Li S, Guo Y, et al. Masked chimeric antigen receptor for tumor-specific activation. Mol Ther 2017;25:274–84.
32. Joo KI, Xiao L, Liu S, Liu Y, Lee CL, Conti PS, et al. Crosslinked multilamellar liposomes for controlled delivery of anticancer drugs. Biomaterials 2013;34:3098–109.
33. Liu Y, Fang J, Kim YJ, Wong MK, Wang P. Codelivery of doxorubicin and paclitaxel by cross-linked multilamellar liposome enables synergistic antitumor activity. Mol Pharm 2014;10:1651–61.
34. Kim Y, Liu Y, Li S, Rohrs J, Zhang R, Zhang X, et al. Co-eradication of breast cancer cells and cancer stem cells by cross-linked multilamellar liposomes enhances tumor treatment. Mol Pharm 2015;12:2811–22.
35. Kochenderfer JN, Feldman SA, Zhao Y, Xu H, Black MA, Morgan RA, et al. Construction and preclinical evaluation of an anti-CD19 chimeric antigen receptor. J Immunother 2009;32:689–702.
36. Li S, Siriwon N, Zhang X, Yang S, Jin T, He F, et al. Enhanced cancer immunotherapy by chimeric antigen receptor-modified T cells engineered to secrete checkpoint inhibitors. Clin Cancer Res 2017;23:6982–92.
37. Moon EK, Wang LC, Dolfi DV, Wilson CB, Ranganathan R, Sun J, et al. Multifactorial T-cell hypofunction that is reversible can limit the efficacy of chimeric antigen receptor-transduced human T cells in solid tumors. Clin Cancer Res 2014;20:4262–73.
38. Mitchell M, King M. Leukocytes as carriers for targeted cancer drug delivery. Expert Opin Drug Deliv 2015;3:375–92.
39. Irvine D, Hanson M, Rakhra K, Tokatlian T. Synthetic nanoparticles for vaccines and immunotherapy. Chem Rev 2015;115:11109–46.
40. Ishida T, Harashima H, Kiwada H. Liposome clearance. Biosci Rep 2002;22:197–224.
41. Longmire M, Choyke PL, Kobayashi H. Clearance properties of nano-sized particles and molecules as imaging agents: considerations and caveats. Nanomedicine (Lond) 2008;3:703–17.
42. Boissonnas A, Fetler L, Zeelenberg IS, Hugues S, Amigorena S. In vivo imaging of cytotoxic T cell infiltration and elimination of a solid tumor. J Exp Med 2007;204:345–56.
43. Iwai Y, Hamanishi J, Chamoto K, Honjo T. Cancer immunotherapies targeting the PD-1 signaling pathway. J Biomed Sci 2017;24:26.
44. Bonifant CL, Jackson HJ, Brentjens RJ, Curran KJ. Toxicity and management in CAR T-cell therapy. Mol Ther Oncolytics 2016;3:16011.
45. Siegler EL, Kim YJ, Chen X, Siriwon N, Mac J, Rohrs JA, et al. Combination cancer therapy using chimeric antigen receptor-engineered natural killer cells as drug carriers. Mol Ther 2017;25:2607–19.
46. Loi S, Pommey S, Haibe-Kains B, Beavis PA, Darcy PK, Smyth MJ, et al. CD73 promotes anthracycline resistance and poor prognosis in triple negative breast cancer. Proc Natl Acad Sci U S A 2013;110:11091–6.
47. Ohta A. A metabolic immune checkpoint: adenosine in tumor microenvironment. Front Immunol 2016;7:109.
48. Blay J, White TD, Hoskin DW. The extracellular fluid of solid carcinomas contains immunosuppressive concentrations of adenosine. Cancer Res 1997;57:2602–5.
49. Montalbán Del Barrio I, Penski C, Schlahsa L, Stein RG, Diessner J, Wöckel A, et al. Adenosine-generating ovarian cancer cells attract myeloid cells which differentiate into adenosine-generating tumor associated macrophages - a self-amplifying, CD39- and CD73-dependent mechanism for tumor immune escape. J Immunother Cancer 2016;4:49.
50. Masopust D, Schenkel JM. The integration of T cell migration, differentiation and function. Nat Rev Immunol 2013;13:309–20.